Report No.
UCB/SEMM-2013/07

Structural Engineering
Mechanics and Materials

Cyclic Steady States of Treaded Rolling Bodies

By

Sanjay Govindjee, Trevor Potter, and Jon Wilkening

July 2013

Department of Civil and Environmental Engineering
University of California, Berkeley

CYCLIC STEADY STATES OF TREADED ROLLING BODIES

SANJAY GOVINDJEE, TREVOR POTTER, AND JON WILKENING

Abstract. The analysis of spinning axisymmetric bodies undergoing finite deformation is useful for understanding the behavior of a wide variety of engineering systems – for example rolling tires. However, progress beyond the axisymmetric case has been lacking. In this work, we present a methodology for the treatment of treaded rolling bodies by devising a shooting scheme for the computation of cyclic steady states of motion. The scheme advocated permits one to determine the entire transient (cyclic) motion of a spinning treaded body with consideration of viscoelasticity as well as contact. We demonstrate the viability of the method through two examples, one a viscoelastic cylinder with eight sinusoidal tread blocks, and one a viscoelastic oval in which repeated contact and separation from a rigid plane excites transient vibrational modes in the body during each cycle.

1. Introduction

The analysis of finitely deformable rolling bodies is an important and well-known problem in engineering. In the case where the body (in the reference configuration) is axisymmetric, important early works include Padovan and Paramodilok [16, 17], Oden and Lin [14], Padovan [15], Bass [3], and Kennedy and Padovan [11]. This literature formulates the equations of motion in the frame of reference of an observer translating alongside the rotating body, who measures deformation at a point as the location of the material point that would have been there were the body rotating rigidly with constant angular velocity. We will refer to this as the "lab frame" and the usual reference configuration as the "material" or "Lagrangian" frame. The lab frame permits a formulation of the equations of motion that allows for finite deformation elastic and viscoelastic stress analysis of the body while in contact with, say, a rigid plane – i.e. a roadway. The solution computed is a true *steady-state* solution; it is strictly time independent in the lab frame.

A major and long-standing shortcoming of this analysis framework is that it strictly requires an axisymmetric reference configuration of the body [13, 7]. Indeed the material properties and geometry of the body must be invariant under rotation about the origin for the equations of motion in the lab frame to be independent of time. In particular, for applications where the rolling body has a tread pattern, the framework outlined above is not applicable since the reference domain in the lab frame would vary in time.

Notwithstanding, if one contemplates the motion of a rolling treaded body, it is apparent that for a wide class of conditions a *cyclic* steady state will often be reached. Consider for example an automobile tire rolling down the road. In principle, for uniform roadways, the state of deformation of the tire will appear the same to an observer moving with the axle

Key words and phrases. treaded, rolling, tires, cyclic steady-state, time-periodic solutions.

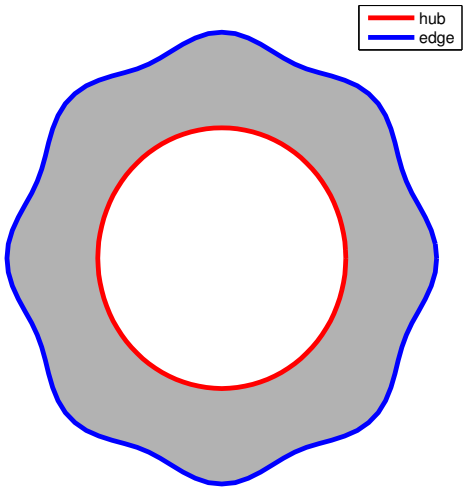

FIGURE 1. The treaded rolling body corresponding to the reference domain $\mathcal{B}_{0.1,8}$.

at the instant that a tread block is in centered contact with the roadway. It matters not which tread block is presently in contact. Furthermore as the tread block rotates, the tire will undergo a dynamic oscillation that will return to the exact same state once the tread block has rotated through any element of the body's symmetry group. One naïve method for dealing with this issue would be to attempt to roll the body (computationally) in a Lagrangian frame from zero velocity up to the the desired rolling velocity and then waiting for the system to settle into the desired cyclic steady state. This brute force approach is certainly valid but requires large computational resources and leaves, as an open question, the difficulty of ensuring that the cyclic steady state has been reached. In the work of Qi et al. [19] a second method of treating the treaded body problem is discussed. However, the method described is proprietary and no detail is provided to allow for a scientific assessment of the procedure. It is the main objective of this work to outline a scheme by which cyclic steady state motions of a rolling body can be computed.

In §2 we review in detail the geometrical modeling of the problem, the relevant boundary conditions, and material modeling assumptions. In §3 we define our scheme for the determination of cyclic steady solutions. The methodology amounts to finding the zero of an expression that measures the difference between the system's state at the start and end of a (defined) period of motion, under the constraint of a system of partial differential equations representing the evolution of the system. We outline our numerical methods in §4 and, in §5, we demonstrate our scheme on a sequence of examples. In §6 we summarize our findings.

2. Constitutive equations and boundary conditions

2.1. **Reference configuration.** For simplicity, we will consider two-dimensional treaded bodies, although our methods also apply to three-dimensional problems. To describe a two-dimensional body, we define a reference domain $\mathcal{B}$ with material points $X = (X_1, X_2)$. We

work in a Lagrangian frame since the reference domain in the lab frame is not stationary in time. Without treads, the two-dimensional body is an annulus about the origin with inner radius r_1 and outer radius r_2. The reference configuration is then given by the set

$$\mathcal{B} = \{(X_1, X_2) \,|\, r_1 \le \|X\|_2 \le r_2\} \,. \tag{2.1}$$

The inner boundary $\Gamma_h = \{X|\ \|X\|_2 = r_1\}$ is called the hub and the outer boundary $\Gamma_e = \{X|\ \|X\|_2 = r_2\}$ is called the edge.

The treadless body above can be seen as the image of the set $A = \{(r,\theta)|\, r_1 \le r \le r_2,\, 0 \le \theta < 2\pi\}$ under the polar coordinate map $T(r,\theta) = (r\cos\theta, r\sin\theta)$. To obtain a body with treads, we perturb $T(r,\theta)$:

$$\begin{aligned} T_{\varepsilon,\beta}(r,\theta) &\stackrel{\text{def}}{=} \psi(r,\varepsilon,\beta)(\cos\theta,\sin\theta) \\ \psi(r,\varepsilon,\beta) &\stackrel{\text{def}}{=} r + \varepsilon(r-r_1)\cos(\beta\theta)\,. \end{aligned} \tag{2.2}$$

The integer β is the number of tread blocks and the parameter ε is the amplitude of the treads relative to the body's size. We then define the reference configuration for the treaded body to be $\mathcal{B}_{\varepsilon,\beta} = T_{\varepsilon,\beta}(A)$ with hub $\Gamma_h = \{T_{\varepsilon,\beta}(r,\theta)\,|\,r = r_1,\, 0 \le \theta < 2\pi\}$ and edge $\Gamma_e = \{T_{\varepsilon,\beta}(r,\theta)\,|\,r = r_2,\, 0 \le \theta < 2\pi\}$. Fig. 1 shows the reference domain for $\beta = 8, \varepsilon = 0.1$. We note that any perturbation of $T(r,\theta)$ can be used; however, we will employ the given smooth perturbations to avoid certain technical issues that would obscure our main purpose. When there is no danger of confusion, we will drop the subscripts from $\mathcal{B}_{\varepsilon,\beta}$ and write $\mathcal{B}$ for the reference configuration.

2.2. **Elastic response.** The motion of the body is given by $\boldsymbol{\phi}(X,t)$ with deformation gradient $\mathbf{F} = \partial\boldsymbol{\phi}/\partial X$. We assume a plane strain elastic response that is described by a compressible Mooney-Rivlin model, with stored energy function $\boldsymbol{\Psi}_e(I_1,I_2,I_3)$ given in terms of the invariants of the three-dimensional right Cauchy-Green tensor $\mathbf{C}_3 = \begin{bmatrix} \mathbf{C} & 0 \\ 0 & 1 \end{bmatrix}$, where $\mathbf{C} = \mathbf{F}^{\mathsf{T}}\mathbf{F}$:

$$\boldsymbol{\Psi}_e = \frac{\kappa}{4}\left(I_3 - \log I_3 - 1\right) + \frac{\mu}{2}(1-s)\left(I_1 - \log I_3 - 3\right) + \frac{\mu}{2}s\left(I_2 - 2\log I_3 - 3\right)\,. \tag{2.3}$$

Here $\kappa > 0$ is the bulk modulus, $\mu > 0$ is the shear modulus, and $s \in [0,1]$ can be chosen to balance the two shear terms. The energy Ψ_e is polyconvex [4, §4.9] and satisfies the conditions for Ball's theory [2] of existence in finite deformation elasticity.

The first Piola-Kirchhoff stress tensor $\mathbf{P}_e$ that arises from $\boldsymbol{\Psi}_e$ is

$$\mathbf{P}_e = \frac{\partial\boldsymbol{\Psi}_e}{\partial\mathbf{F}} = \frac{\kappa}{2}(I_3-1)\mathbf{F}^{-\mathsf{T}} + \mu(1-s)(\mathbf{F}-\mathbf{F}^{-\mathsf{T}}) + \mu s(I_1\mathbf{F} - \mathbf{F}\mathbf{C} - 2\mathbf{F}^{-\mathsf{T}})\,. \tag{2.4}$$

2.3. **Viscoelastic response.** Many popular models of viscoelasticity employ linear evolutions equations for the (large deformation) viscoelastic stresses and we have, indeed, successfully applied our methods in this case [18] using a model of Simo [23]. However, it has been demonstrated in [8], by counterexample, that such models can lead to exponential energy growth and thus may not satisfy the 2nd Law of Thermodynamics. Therefore, here,

we use the viscoelastic model of Reese and Govindjee [9, 21, 20], a nonlinear Sidoroff-class model [22] that has been proven to satisfy the 2nd Law.

The model of Reese and Govindjee is derived [21] by assuming a multiplicative split of the deformation gradient

$$\mathbf{F} = \mathbf{F}_e\mathbf{F}_v \tag{2.5}$$

into an elastic part $\mathbf{F}_e$ and a viscous part $\mathbf{F}_v$. We define a viscoelastic stored energy function $\mathbf{\Psi}_v$ that depends only on the strain associated with the elastic part: $\mathbf{b}_e = \mathbf{F}_e\mathbf{F}_e^{\mathsf{T}}$:

$$\mathbf{\Psi}_v = \nu\left(\frac{\kappa}{4}\left(I_3^e - \log I_3^e - 1\right) + \frac{\mu}{2}(1-s)\left(I_1^e - \log I_3^e - 3\right) + \frac{\mu}{2}s\left(I_2^e - 2\log I_3^e - 3\right)\right), \tag{2.6}$$

where I_1^e, I_2^e, I_e^e are the invariants of the three-dimensional tensor $\mathbf{b}_{3e} = \begin{bmatrix} \mathbf{b}_e & 0 \\ 0 & 1 \end{bmatrix}$ and ν is a parameter that weights the strength of the viscoelastic response. $\mathbf{\Psi}_v$ gives rise to a first Piola-Kirchhoff stress tensor $\mathbf{P}_v$:

$$\begin{aligned}\mathbf{P}_v &= 2\frac{\partial \mathbf{\Psi}_v}{\partial \mathbf{b}_e}\mathbf{b}_e\mathbf{F}^{-\mathsf{T}} \\ &= \nu\left(\frac{\kappa}{2}(I_3^e - 1)\mathbf{I} + \mu(1-s)(\mathbf{b}_e - \mathbf{I}) + \mu s(I_1^e\mathbf{b}_e - \mathbf{b}_e^2 - 2\mathbf{I})\right)\mathbf{F}^{-\mathsf{T}}.\end{aligned} \tag{2.7}$$

In order to have a closed system, the dynamics of the internal variable $\mathbf{b}_e$ must be specified:

$$\dot{\mathbf{b}_e} = \boldsymbol{\ell}\mathbf{b}_e + \mathbf{b}_e\boldsymbol{\ell}^{\mathsf{T}} - 2\mathcal{V}(\boldsymbol{\tau}_e)\mathbf{b}_e\,, \tag{2.8}$$

where

$$\begin{aligned}\boldsymbol{\ell} = \dot{\mathbf{F}}\mathbf{F}^{-1}, \qquad \boldsymbol{\tau}_e = 2\frac{\partial \mathbf{\Psi}_v}{\partial \mathbf{b}_e}\mathbf{b}_e \\ \mathcal{V}(\boldsymbol{\tau}_e) = \frac{1}{2\mu\tau}\left(\boldsymbol{\tau}_e - \frac{1}{2}(\operatorname{tr}\boldsymbol{\tau}_e)\mathbf{I}\right) + \frac{1}{4\kappa\tau}(\operatorname{tr}\boldsymbol{\tau}_e)\mathbf{I}\,.\end{aligned} \tag{2.9}$$

Note that τ is a viscoelastic relaxation time parameter, while $\boldsymbol{\tau}_e$ is the Kirchhoff stress tensor corresponding to $\mathbf{P}_v$.

Finally, we define the total first Piola-Kirchhoff stress tensor to be the sum of the elastic and viscoelastic stress tensors:

$$\mathbf{P} = \mathbf{P}_e + \mathbf{P}_v\,. \tag{2.10}$$

Assuming constant Dirichlet or Neumann boundary conditions, a computation shows that the total stored energy function $\mathbf{\Psi} = \mathbf{\Psi}_e + \mathbf{\Psi}_v$ satisfies the 2nd Law of Thermodynamics and may be used to construct a Lyapunov function of the dynamical system.

2.4. **Boundary conditions.** We imagine the body is being spun at a constant speed ω along the hub so that

$$\boldsymbol{\phi}(X,t) = \mathbf{R}(t)X \text{ on } \Gamma_h\,, \tag{2.11}$$

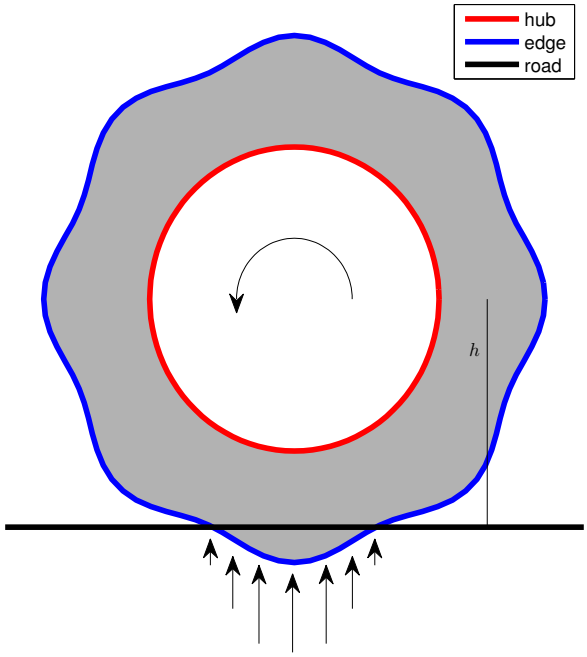

FIGURE 2. Illustration of the positioning of the road and the traction forces experienced on the edge. The traction increases in magnitude the deeper the body penetrates the road. The direction of rotation is also indicated.

where $\mathbf{R}(t)$ is the rotation matrix given by $\begin{bmatrix} \cos(\omega t) & -\sin(\omega t) \\ \sin(\omega t) & \cos(\omega t) \end{bmatrix}$. On the edge, there is either a free surface or the body is in contact with the road (or other stiff surface). The free surface is described by the absence of traction along that part of the boundary of the reference configuration. It is given by the formula $\mathbf{PN} = \mathbf{0}$.

We model contact with the road by prescribing a simple penalty force pushing against the edge of the body, if the edge penetrates beneath the surface of the road (see Fig. 2). More specifically, let $h > r_1$ be the distance from the x-axis to the road, so that the road is lying along $y = -h$. If X is a point on the edge and $x_2 = \boldsymbol{\phi}_2 = \boldsymbol{\phi}_2(X) < -h$, we consider a force of magnitude $\delta\gamma(-h - x_2)$ per unit reference area in the x_2 direction, $\mathbf{e}_2$. We require that $\gamma(0) = 0$ and that $\gamma(z)$ is monotonically increasing for $z > 0$. The parameter $\delta > 0$ will be chosen to ensure that the road is sufficiently stiff. The specific choice of γ will be discussed in §5. The traction force is applied at the point $x = \boldsymbol{\phi}(X)$ in the deformed configuration. In precise terms: at a point X on the edge with outward normal $\mathbf{N}$ of the reference configuration, we have

$$\mathbf{PN} = \delta\gamma(-h - x_2)\mathbf{e}_2\,. \tag{2.12}$$

The free boundary condition and the road boundary condition on the edge can be expressed as the single condition

$$\mathbf{PN} = \delta\gamma(-h - x_2)\mathbf{e}_2\,, \tag{2.13}$$

by choosing γ such that $\gamma(z) = 0$ for $z \leq 0$. For later convenience we define

$$\mathbf{h} = \delta\gamma(-h - x_2)\mathbf{e}_2\,. \tag{2.14}$$

2.5. **Equations of motion.** The motion is given by

$$\begin{aligned} \rho_R\ddot{\boldsymbol{\phi}} &= \operatorname{DIV}\mathbf{P} && \text{on } \mathcal{B} \\ \dot{\mathbf{b}}_e &= \boldsymbol{\ell}\mathbf{b}_e + \mathbf{b}_e\boldsymbol{\ell}^{\mathsf{T}} - 2\mathcal{V}(\boldsymbol{\tau}_e)\mathbf{b}_e && \text{on } \mathcal{B}\,, \end{aligned} \tag{2.15}$$

with boundary conditions

$$\begin{aligned} \boldsymbol{\phi}(X,t) &= \mathbf{R}(t)X && \text{on } \Gamma_h \\ \mathbf{PN} &= \mathbf{h} && \text{on } \Gamma_e\,. \end{aligned} \tag{2.16}$$

We reduce the second order equation to a system of first order equations by introducing the velocity of the motion, $\boldsymbol{\nu}(X,t)$ as an independent field variable. The equations of motion on $\mathcal{B}$ then become:

$$\begin{aligned} \dot{\boldsymbol{\phi}} &= \boldsymbol{\nu} \\ \dot{\boldsymbol{\nu}} &= \frac{1}{\rho_R}\operatorname{DIV}\mathbf{P} \\ \dot{\mathbf{b}}_e &= \boldsymbol{\ell}\mathbf{b}_e + \mathbf{b}_e\boldsymbol{\ell}^{\mathsf{T}} - 2\mathcal{V}(\boldsymbol{\tau}_e)\mathbf{b}_e\,, \end{aligned} \tag{2.17}$$

with boundary conditions

$$\begin{aligned} \boldsymbol{\phi}(X,t) &= \mathbf{R}(t)X && \text{on } \Gamma_h \\ \boldsymbol{\nu}(X,t) &= \dot{\mathbf{R}}(t)X && \text{on } \Gamma_h \\ \mathbf{PN} &= \mathbf{h} && \text{on } \Gamma_e\,. \end{aligned} \tag{2.18}$$

The weak formulation of the equations of motion, which we will need later for finite element analysis, are

$$\begin{aligned} \int_{\mathcal{B}} \dot{\boldsymbol{\phi}}\cdot\zeta &= \int_{\mathcal{B}} \boldsymbol{\nu}\cdot\zeta \\ \int_{\mathcal{B}} \dot{\boldsymbol{\nu}}\cdot\eta &= \int_{\mathcal{B}} -\frac{1}{\rho_R}\mathbf{P} : D\eta + \int_{\Gamma_e}\frac{1}{\rho_R}\mathbf{h}\cdot\eta \\ \int_{\mathcal{B}} \dot{\mathbf{b}}_e : K &= \int_{\mathcal{B}} \left(\boldsymbol{\ell}\mathbf{b}_e + \mathbf{b}_e\boldsymbol{\ell}^{\mathsf{T}} - 2\mathcal{V}(\boldsymbol{\tau}_e)\mathbf{b}_e\right) : K\,. \end{aligned} \tag{2.19}$$

Here ζ, η and K are arbitrary test functions, with K being symmetric tensor-valued. The test functions ζ and η are required to be $\mathbf{0}$ on the hub, Γ_h. When convenient, we will denote the triple $(\boldsymbol{\phi}, \boldsymbol{\nu}, \mathbf{b}_e)$ by $\mathbf{z}$.

2.6. **Linearization.** We will need the linearization of the weak form equations, in order to apply Newton's method. We will use the following notation: given a function f of $\mathbf{z}$ and a tangent $\hat{\mathbf{z}}$, we denote the derivative of $f(\mathbf{z})$ in the direction of $\hat{\mathbf{z}}$ as $\widehat{f}$. Precisely,

$$\widehat{f} \stackrel{\text{def}}{=} \frac{d}{d\varepsilon}\Big|_{\varepsilon=0} f(\mathbf{z} + \varepsilon\hat{\mathbf{z}})\,. \tag{2.20}$$

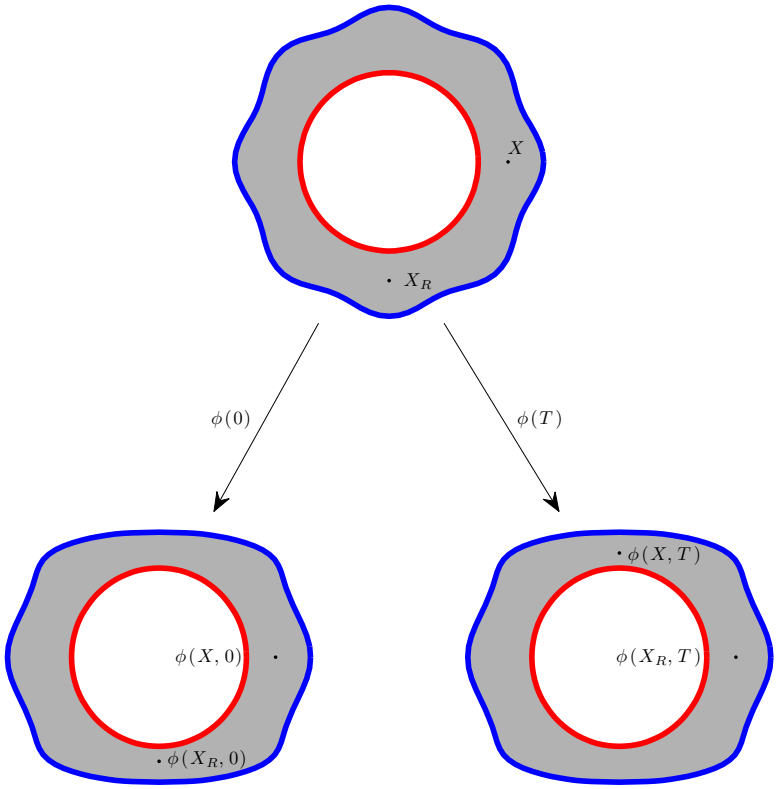

FIGURE 3. The top figure is the reference configuration with material points X and $X_R = \mathbf{R}^{\mathsf{T}}(T)X$. Bottom left is the deformed configuration at time 0. Bottom right is the deformed configuration at time T, for which the body is the same state as at time 0. We observe that $\boldsymbol{\phi}(X_R, T) = \boldsymbol{\phi}(X, 0)$.

With this notation, the linearized weak form equations become

$$
\begin{aligned}
\int_{\mathcal{B}} \dot{\widehat{\boldsymbol{\phi}}} \cdot \zeta &= \int_{\mathcal{B}} \widehat{\boldsymbol{\nu}} \cdot \zeta \\
\int_{\mathcal{B}} \dot{\widehat{\boldsymbol{\nu}}} \cdot \eta &= \int_{\mathcal{B}} -\frac{1}{\rho_R} \widehat{\mathbf{P}} : D\eta + \int_{\Gamma_e} \frac{1}{\rho_R} \widehat{\mathbf{h}} \cdot \eta \\
\int_{\mathcal{B}} \dot{\widehat{\mathbf{b}}}_e : K &= \int_{\mathcal{B}} \left(\widehat{\boldsymbol{\ell} \mathbf{b}_e} + \widehat{\mathbf{b}_e \boldsymbol{\ell}^{\mathsf{T}}} - 2\widehat{\mathcal{V}(\boldsymbol{\tau}_e)\mathbf{b}_e} \right) : K \, .
\end{aligned}
\tag{2.21}
$$

with boundary conditions $\widehat{\boldsymbol{\phi}} = \widehat{\boldsymbol{\nu}} = \mathbf{0}$ on Γ_h.

See Appendix A for a detailed computation of the terms $\widehat{\mathbf{P}}, \dot{\widehat{\mathbf{b}}}_e$, and $\widehat{\mathbf{h}}$.

3. CYCLIC STEADY STATES

With the equations of motion in hand, we turn to finding cyclic steady states of the treaded body. Other systems in which time-periodic solutions of partial differential equations are of interest include Couette turbulence [24], integrable equations [1], mode-locked

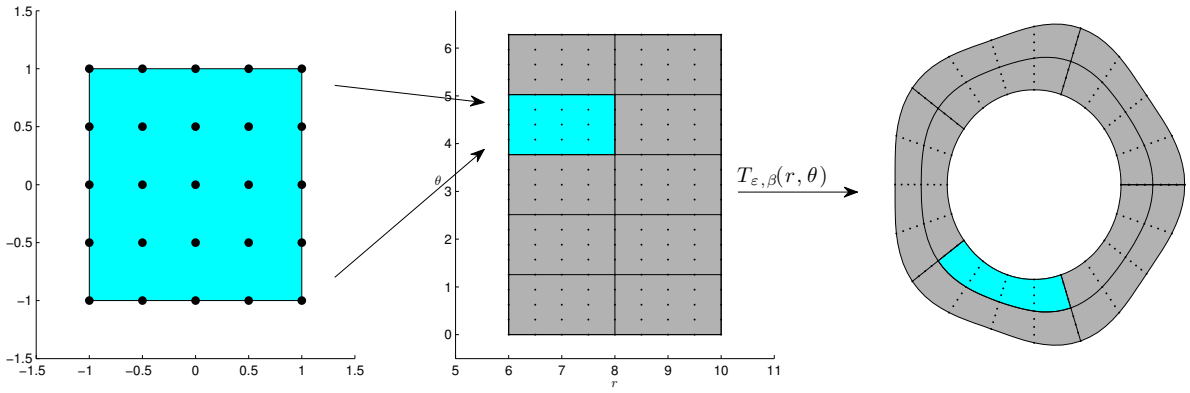

FIGURE 4. The reference element is mapped to the r-θ plane, where it is then mapped by $T_{\varepsilon,\beta}$ onto the reference configuration $\mathcal{B}_{\varepsilon,\beta}$.

lasers [26], and surface water waves [25]. Below, we adopt a similar mathematical framework as in those works.

We seek solutions of (2.19) that return to the same state as their initial configuration after some time T. This corresponds to searching for a solution $\mathbf{z} = (\boldsymbol{\phi}, \boldsymbol{\nu}, \mathbf{b}_e)$ that satisfies

$$\begin{aligned} \boldsymbol{\phi}(\mathbf{R}^{\mathsf{T}}(T)X, T) &= \boldsymbol{\phi}(X, 0) \\ \boldsymbol{\nu}(\mathbf{R}^{\mathsf{T}}(T)X, T) &= \boldsymbol{\nu}(X, 0) \\ \mathbf{b}_e(\mathbf{R}^{\mathsf{T}}(T)X, T) &= \mathbf{b}_e(X, 0)\,; \end{aligned} \tag{3.1}$$

see Fig. 3. For a body with no treads, the above equations make sense for any value of T, and by solving them for all T simultaneously, one would obtain the steady rolling state of the body. This cannot be done for a treaded body, since T must be an integer multiple of $2\pi/(\omega\beta)$, where β is the number of tread blocks. In this case, we refer to a solution of (3.1) as a cyclic steady state. In general, one may expect to find different dynamics for different choices of T, but in the viscoelastic case, we observe a single cyclic steady state for any admissible choice of T.

We rewrite the equations (3.1) as a function of an initial condition $\mathbf{z}_0 = (\boldsymbol{\phi}_0, \boldsymbol{\nu}_0, (\mathbf{b}_e)_0)$:

$$\mathcal{H}_T(\mathbf{z}_0) = \mathbf{z}(\mathbf{R}^{\mathsf{T}}(T)X, T) - \mathbf{z}_0\,, \tag{3.2}$$

where $\mathbf{z}(X,t)$ evolves according to (2.19) with initial condition $\mathbf{z}_0$. We can now search for cyclic steady states by finding a solution to $\mathcal{H}_T(\mathbf{z}_0) = \mathbf{0}$. To find a $\mathbf{0}$ of $\mathcal{H}_T$, we will also require its derivative:

$$D\mathcal{H}_T[\mathbf{z}_0](\hat{\mathbf{z}}_0) = \hat{\mathbf{z}}(\mathbf{R}^{\mathsf{T}}(T)X, T) - \hat{\mathbf{z}}_0\,, \tag{3.3}$$

where $\hat{\mathbf{z}}(X,t)$ evolves according to the linearized equations (2.21) with initial condition $\hat{\mathbf{z}}_0$.

4. Numerical methods

We now describe the numerical methods employed to discretize and then solve $\mathcal{H}_T(\mathbf{z}_0) = \mathbf{0}$. We employ quartic quadrilateral C_0 iso-geometric elements to discretize the weak equations as in Fig. 4. We use a structured mesh that is mapped to the reference configuration via $T_{\varepsilon,\beta}$. The numerical degrees of freedom are given by the coefficients of the finite element basis functions used to represent $\boldsymbol{\phi}$, $\boldsymbol{\nu}$, and $\mathbf{b}_e$. The requisite mass matrix solves are performed iteratively using conjugate gradients, which typically converges in 50 iterations independent of problem size. We evolve the discretized equations in time using an 8th order explicit Runge-Kutta method of Dormand and Prince [10, 6]. In addition to being high order, this method has a larger stability region than lower order explicit Runge-Kutta methods, which is useful since we have found the equations to be moderately stiff. We compared its performance with Dormand and Prince's 5th order method [5], and found that the two methods required very similar computational effort to achieve stability, but the higher order method was more accurate.

With the above numerical techniques we can compute $\mathbf{z}(X,T)$ given an initial condition $\mathbf{z}_0$. But to discretize $\mathcal{H}_T$, we must compute $\mathbf{z}(\mathbf{R}^\mathsf{T}X,T)$. We choose the number of elements in the circumferential direction, e_c, to be a multiple of β, the number of tread blocks, so that we can compute $\mathbf{z}(\mathbf{R}^\mathsf{T}X,T)$ by shifting the values of $\mathbf{z}(X,T)$ at the nodes. Specifically, if after time T the body has rotated over n tread blocks, we shift the values at the nodes by $n\beta/e_c$ elements counterclockwise.

We denote the discretization of $\mathcal{H}_T$ by $\bar{\mathcal{H}}_T$ and denote its derivative, taken about a point $\mathbf{z}_0$, by $D\bar{\mathcal{H}}_T[\mathbf{z}_0]$. $\bar{\mathcal{H}}_T = \mathbf{0}$ is solved using Newton's method. Assuming a solution $\mathbf{z}_0^{(*)}$ that satisfies $\bar{\mathcal{H}}_T(\mathbf{z}_0^{(*)}) = \mathbf{0}$ and a first approximation to $\mathbf{z}_0^{(*)}$, $\mathbf{z}_0^{(0)}$, Newton's method produces successive approximations $\mathbf{z}_0^{(i)}$ by the following procedure:

$$\begin{aligned} &\text{Solve} \quad D\bar{\mathcal{H}}_T[\mathbf{z}_0^{(i)}](\hat{\mathbf{z}}_0^{(i)}) = -\bar{\mathcal{H}}_T(\mathbf{z}_0^{(i)}) \quad \text{for } \hat{\mathbf{z}}_0^{(i)}\,. \\ &\text{Set} \qquad\qquad\qquad \mathbf{z}_0^{(i+1)} = \mathbf{z}_0^{(i)} + \hat{\mathbf{z}}_0^{(i)}\,. \end{aligned} \tag{4.1}$$

To solve for $\hat{\mathbf{z}}_0^{(i)}$ in (4.1), we employ the iterative solver GMRES, which finds an approximate solution to the linear equation $Ax = b$ using only matrix-vector products. See [12] for an introduction to this and other Newton-Krylov methods. We choose this approach over a direct solve, which we implemented but found expensive. Indeed, forming the matrix corresponding to $D\bar{\mathcal{H}}_T[\mathbf{z}_0^{(i)}]$ is an $\mathcal{O}(n^2k)$ operation and directly solving it is an order $\mathcal{O}(n^3)$ operation, where n is the number of spatial degrees of freedom and k is the number of time steps. By contrast, the GMRES algorithm is $\mathcal{O}(n(k+m)m)$, where m is the number of GMRES iterations performed (typically 12). In either approach, the constants in the operation counts involving k are quite large due to the number of internal Runge-Kutta stages and the use of conjugate gradients on the mass matrix.

We briefly describe the GMRES algorithm applied to our Newton procedure (4.1). We compute an orthonormal basis for $\operatorname{span}\{b, Ab, A^2b, \ldots, A^mb\}$ with $A = D\bar{\mathcal{H}}_T[\mathbf{z}_0^{(i)}]$ and $b = -\bar{\mathcal{H}}_T(\mathbf{z}_0^{(i)})$. The minimizer of the residual $\|Ax-b\|_2$ over this subspace gives the approximate solution to the linear system, which we set to be $\hat{\mathbf{z}}_0^{(i)}$.

To compute a basis for span$\{b, Ab, A^2b, \ldots, A^mb\}$, we must apply the operator $D\bar{\mathcal{H}}_T[\mathbf{z}_0^{(i)}]$ to multiple inputs. Specifically, we first compute the solution $\mathbf{z}(X,t)$ of the nonlinear equations (2.19) with initial condition $\mathbf{z}_0^{(i)}$ and then evolve the equations linearized about $\mathbf{z}$, (2.21), for multiple initial conditions, i.e. those that arise when forming the Krylov vectors. Since the values of $\mathbf{z}(X,t)$ are needed to evolve the linearized equations, the values of $\mathbf{z}(X,t)$ are stored for all time steps and interpolated (to 8th order, [10]) as needed by the Runge-Kutta time-stepper for the linearized equations. Alternatively, one can avoid interpolation by re-evolving the nonlinear equations along with the linearized ones [25].

5. Results

5.1. **Units and constants.** Our choice of units is Newtons (N), megagrams (Mg), and seconds (s). This choice implies the unit for length is millimeters (mm).

In the remainder of the results section, we will use the following values for constants, unless otherwise noted. The body has inner radius $r_1 = 240$ mm and outer radius $r_2 = 400$ mm. The density of the body is $\rho = 1 \times 10^{-9}$ Mg/mm^3. The bulk modulus κ and shear modulus μ are 689 N/mm^2 and 6.89 N/mm^2, respectively. The dimensionless viscous strength parameter ν has value 1 and the relaxation time is 0.01 seconds. The distance from the axis to the road, h, is 380 mm and the road stiffness parameter δ is 1000 N/mm^2. The body's tread thickness parameter ε is 0.1 and the number of treads β is 8.

We must also define the road force function $\gamma(x)$, which should be monotonically increasing for $x > 0$ and satisfy $\gamma(x) = 0$ for $x \le 0$. A simple choice would be

$$\left\{ \begin{array}{rcll} \gamma(x) &=& 0, & x \le 0 \\ \gamma(x) &=& x, & x \ge 0\,. \end{array} \right. \tag{5.1}$$

However, this choice of γ is not smooth and will lead to non-smooth discretized equations. Instead we choose the smooth function

$$\left\{ \begin{array}{rcll} \gamma(x) &=& 0, & x \le 0 \\ \gamma(x) &=& \exp(x - x^{-1}), & x \ge 0\,. \end{array} \right. \tag{5.2}$$

This function has the drawback of converging to zero exponentially fast as $x \to 0$ from the right, resulting in an weak road force for small road penetration. This trade-off between smoothness and enforcement of constraints arises frequently in contact problems.

5.2. **Example computation of a cyclic steady state.** Figures 5–9 show the results of a typical computation of a cyclic steady state of a treaded body. The mesh size is $e_c = 32$, $e_r = 4$. The body has $\beta = 8$ treads and is rotating with frequency $\omega = 10$ rad/s. We rotate the body over one tread block, which implies $T = 2\pi/(\beta\omega)$.

We take 10000 time steps to evolve the weak equations and the linearized weak equations. This number is chosen to be big enough that the time stepping remains stable. We have found that with the 8th order method, the number of timesteps required for stability is also sufficient to ensure that the temporal discretization is fully converged.

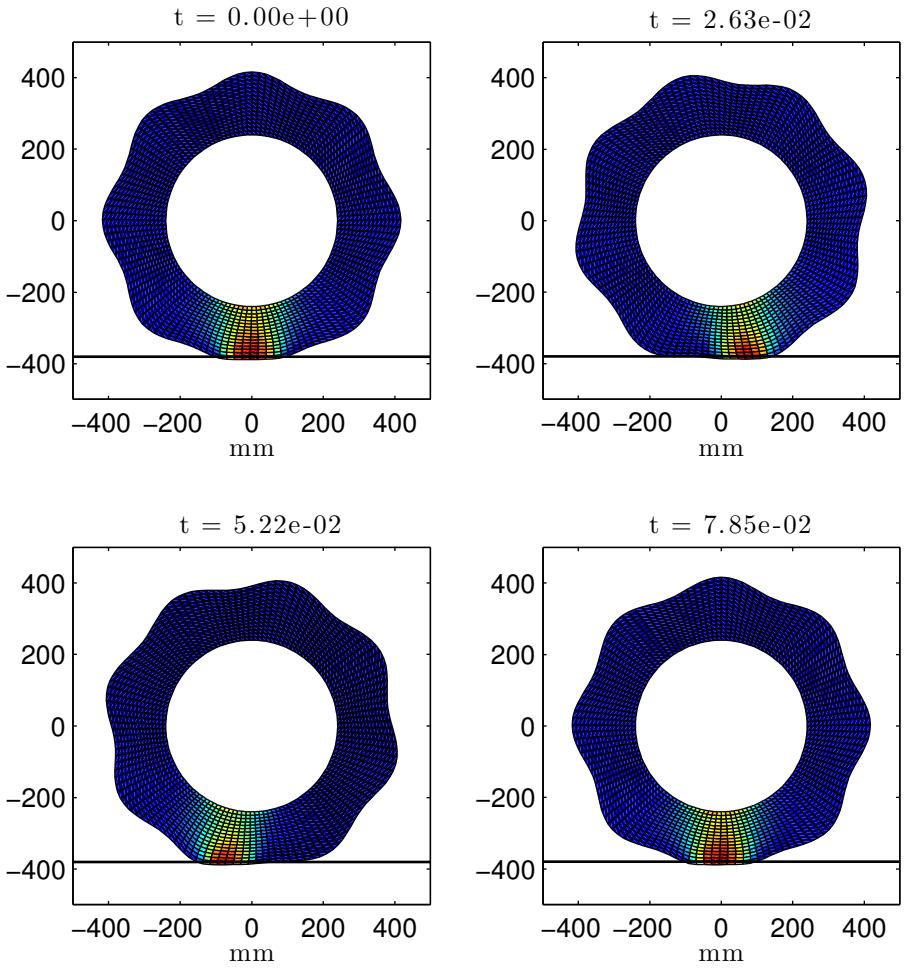

FIGURE 5. Plot of the body as it rotates counterclockwise from one tread to the next. Red indicates high first principal stress while blue indicates low first principal stress.

We first perform a static calculation to determine the deformation of the body at rest when pressed against the road. This is used as an initial guess for Newton's method, which solves the cyclic steady state equations for the rotating body to approximately 8 digits of accuracy. Within each Newton iteration, GMRES performs linear solves on the Jacobian of $\bar{\mathcal{H}}_T$. Setting the tolerance on the GMRES residual to 1×10^{-3} is sufficient for Newton's method to perform well and obtain super-linear convergence. A typical number of GMRES iterations for this tolerance is 12 and a typical number of Newton iterations is 5.

The GMRES algorithm dominates the computation. Each iteration requires approximately 15 minutes on 32 processors, hence the entire simulation requires approximately $15 \times 5 \times 12$ minutes $= 15$ hours.

It is also possible to incrementally increase the road strength, rotation speed, or tread amplitude until the desired values are reached but we found this unnecessary in the above computation.

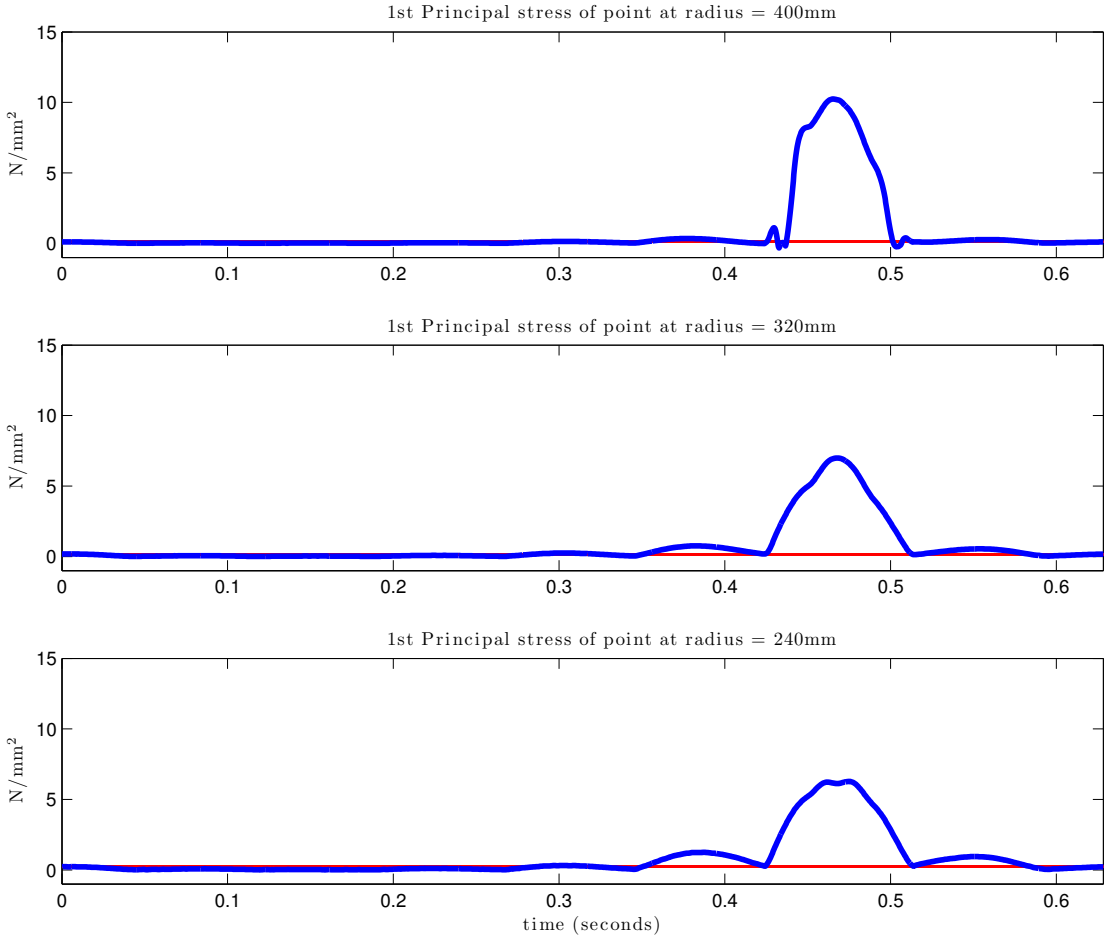

FIGURE 6. Plots of the evolution of the first principal stress over one revolution. The plots represent points at different distances from the hub, from furthest to closest. The constant lines indicate the initial and final values in each plot, which are equal due to time-periodicity.

5.3. **Time evolution of stress of the treaded body.** After computing a cyclic steady state for the treaded body, we compute the first principal stress at various locations. Fig. 5 shows the principal stress of the body at various points in time, while Fig. 6 shows the first principal stresses at a material point as it makes one full revolution around the body. At time $t = 0$ the material point begins on the positive x-axis. The first principal stress spikes as the material point passes near the road. The first principal stress is largest at the outer boundary of the body where contact with the road is made. We note that the slight double peak in the first principal stress for a material point on the hub occurs because of high shear stresses on either side of the portion of the hub closest to the road.

Fig. 7 quantifies the difference in stresses at different points along a tread. The first principal stress decreases as we move from the tread crest to the tread trough. We note that the first principal stress at the tread trough is appreciable in size when the adjacent tread crests are in contact with the road (approximately during time intervals $[0.3, 0.4]$ s

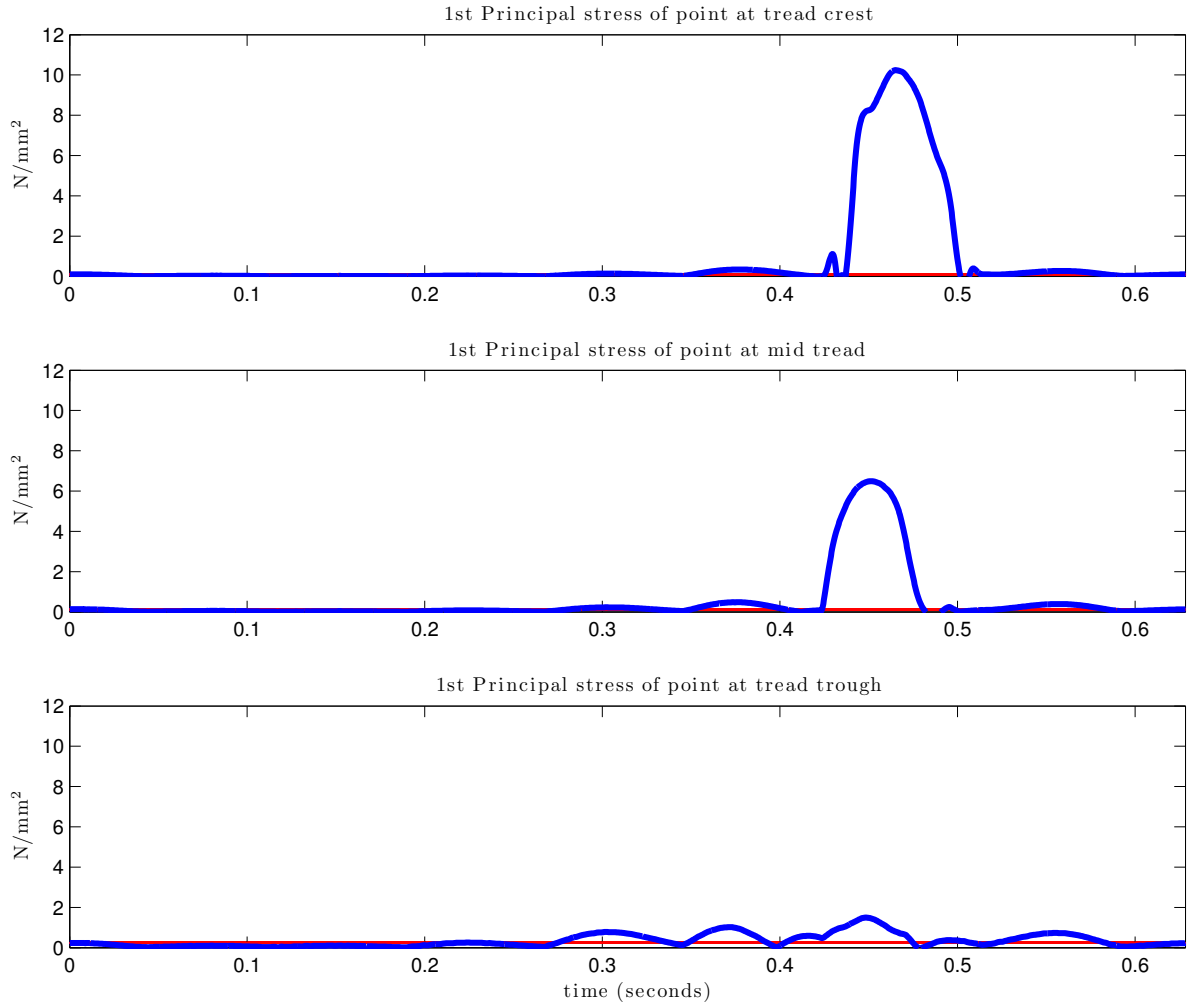

FIGURE 7. Plots of the evolution of the first principal stress over one revolution. The plots represent points at different locations along the edge of the body. The top plot is at a tread peak, the bottom plot is at a tread trough, and the middle plot is midway between. The constant lines correspond to the initial and final values in each plot.

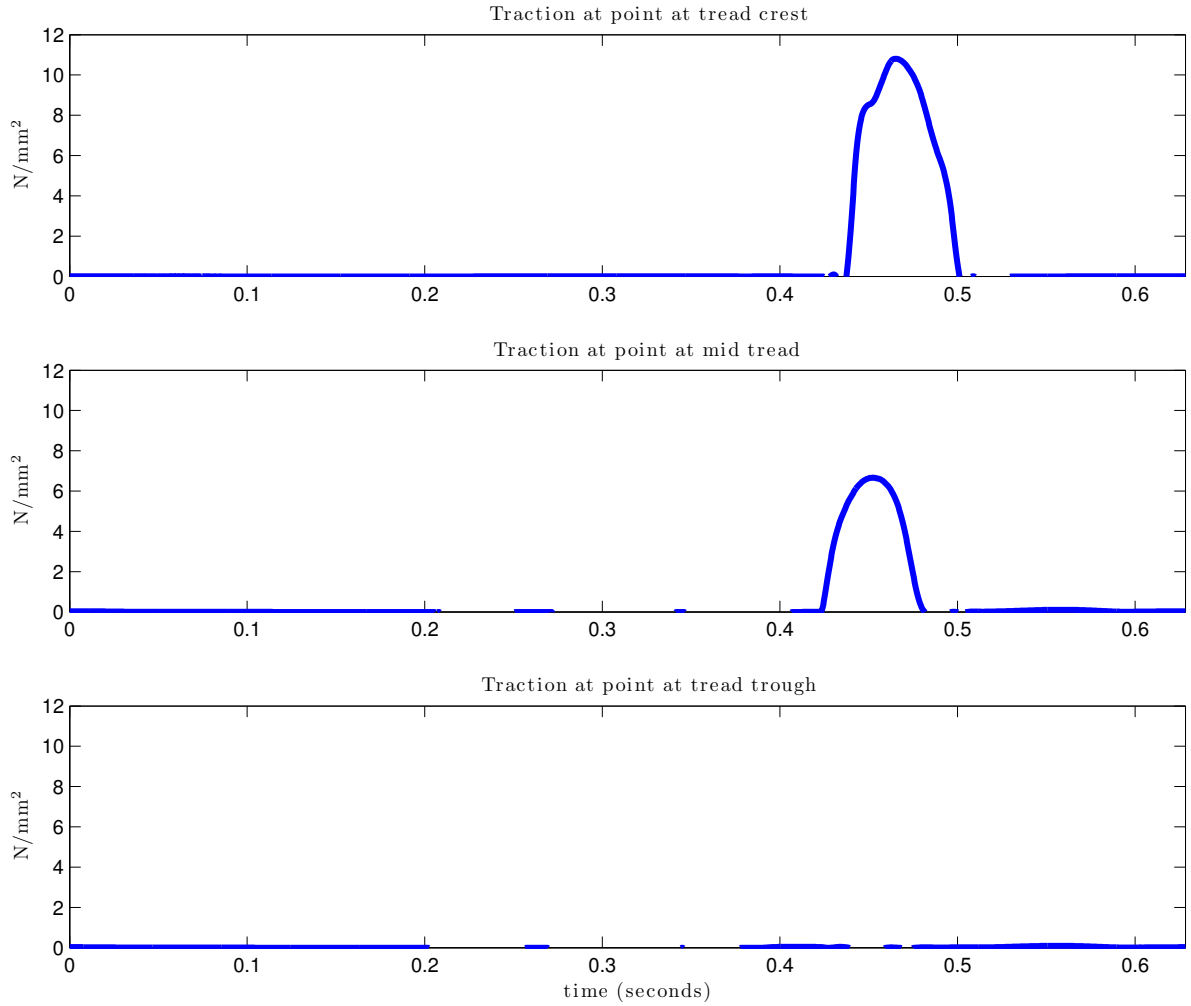

FIGURE 8. Plots of traction over one revolution. The plots represent points at different locations along the edge of the body. The top plot is at a tread peak, the bottom plot is at a tread trough, and the middle plot is midway between.

and $[0.5, 0.6]$ s in the bottom plot in Fig. 7). This is caused by the tread trough being squeezed by the adjacent treads due to its concave geometry.

We plot the magnitude of the traction experienced by a material point along the edge as it rotates with the body in Fig. 8. As might be expected, the traction is largest at the tread peak and smallest at the tread trough when the point passes over the road.

In Fig. 9 we observe the shear stress along the hub, specifically $\mathbf{PN} \cdot \mathbf{t}$, where $\mathbf{N}$ is the outward normal pointing into the hub and $\mathbf{t}$ is the tangent vector along the hub in the counterclockwise direction. This figure indicates that the largest shear stresses on the hub occur radially inline with the tread troughs.

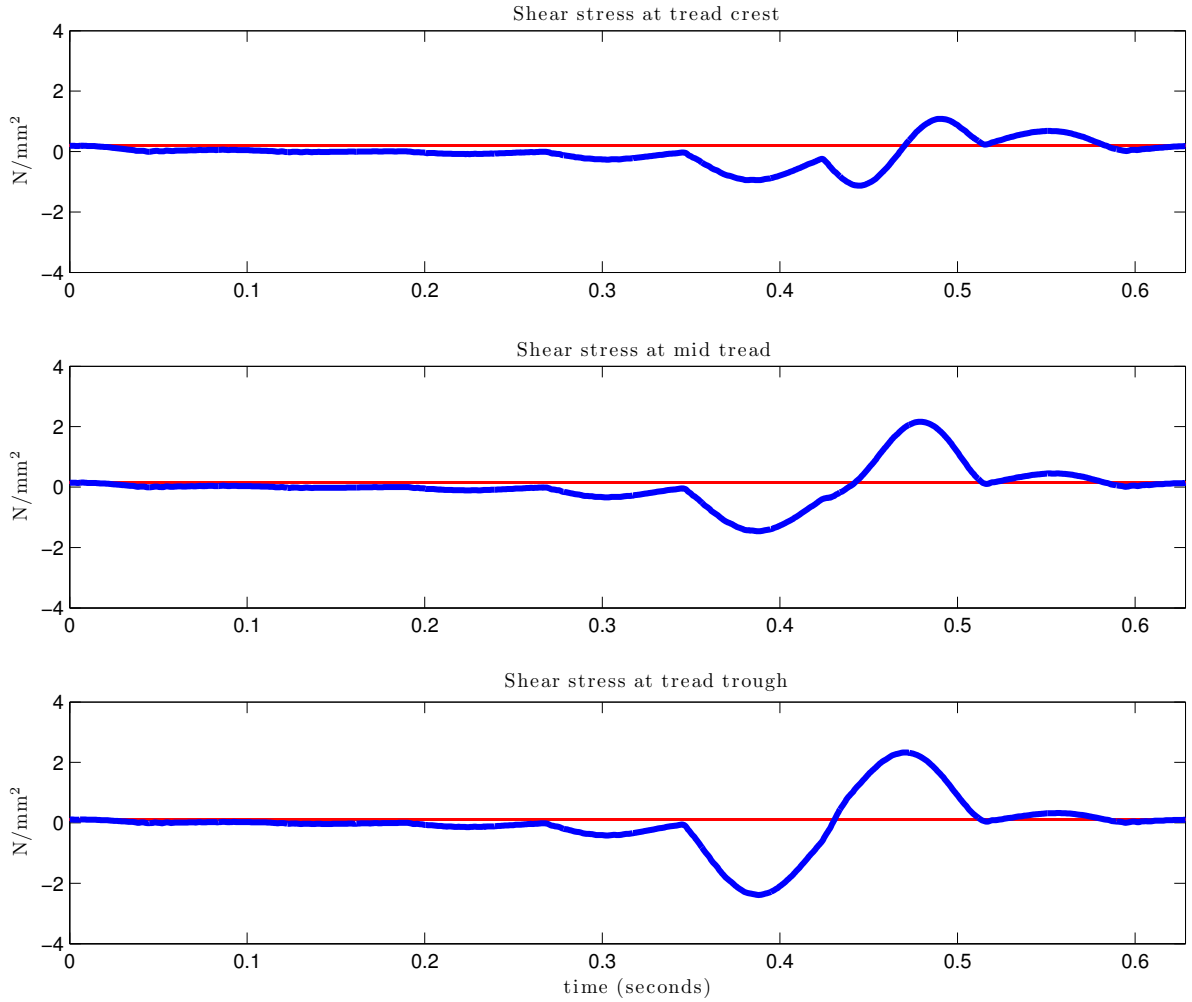

FIGURE 9. Plots of shear stresses of material points along the hub over one revolution. The plots represent points at different locations along the hub. The top plot is radially in line with a tread peak, the bottom plot with a tread trough, and the middle plot is midway between. The constant lines indicate the initial and final values, which are equal due to time-periodicity.

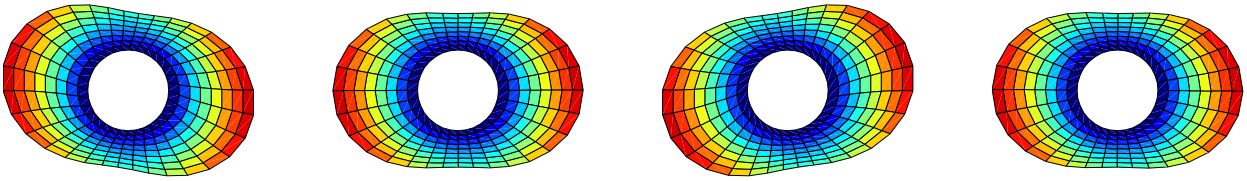

FIGURE 10. Plots of a simple oscillating mode of the oval over one period.

5.4. **A rotating viscoelastic oval.** We now consider an example where the numerical method for finding cyclic steady states can capture the natural damped oscillations of a viscoelastic body. This demonstrates that the cyclic steady state framework can accurately capture motions that would not be present in any steady state calculation.

Consider a rotating oval-shaped body, which is modeled in the our framework by setting $\beta = 2, \varepsilon = 0.4$. The oval is spun at 20 rad/s and can collide with the road, which we expect to excite vibrations. By computing the smallest eigenvalue and corresponding eigenvector of the oval when stationary, we observe the fundamental mode (see Fig. 10) which has a period of oscillation of approximately 1.7×10^{-2} seconds.

We compute a cyclic steady state solution for half a revolution of the oval, which has a half-period of approximately 0.15 seconds and hence ample time to observe oscillations of the fundamental mode. The computed cyclic steady state solution shows that the fundamental mode is excited as the oval contacts the road. In Fig. 11 we see good agreement between the angular displacement of the computed cyclic steady state of the oval and the oscillations predicted by the fundamental mode analysis.

6. CONCLUSION

The analysis of spinning and rolling non-axisymmetric bodies undergoing finite deformation has been an outstanding computational problem. In this work we have outlined a scheme for computing their cyclic steady states that does not involve rolling the body in a Lagrangian frame from zero velocity to its final speed and then waiting for it to settle into a cyclic steady state. The central idea was to note that the essence of the question is to determine an *initial condition* of the body that results in a time evolved state at the end of a (fixed) period which is identical to the initial condition. This permits one to construct a residual expression that must be zero for a cyclic steady state. The zero of this residual is then found under the constraint of the partial differential equations that govern the time evolution of the rotating body's motion and internal state variables. The scheme has been demonstrated on a set of simple examples in order to illustrate its viability and to highlight the types of technical response quantities that can be computed from such a methodology.

Acknowledgments. T.P. and J.W. were supported in part by the Director, Office of Science, Computational and Technology Research, U.S. Department of Energy under Contract No. DE-AC02-05CH11231 and by the National Science Foundation under Grant No. DMS-0955078. Any opinions, findings, and conclusions or recommendations expressed in this

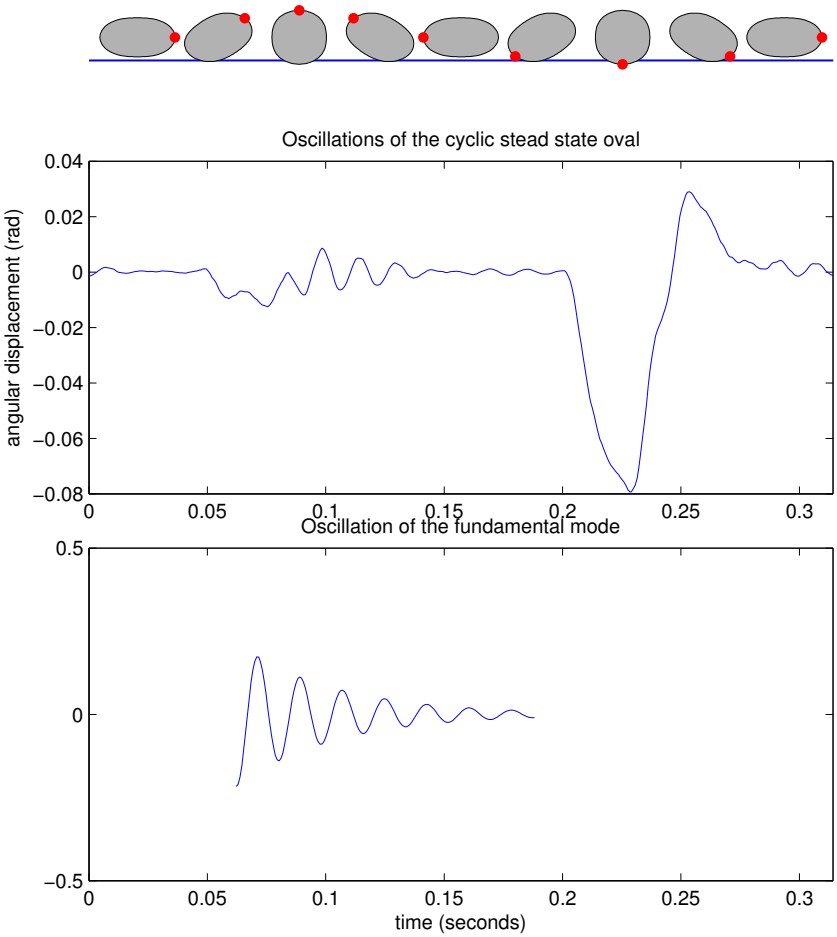

FIGURE 11. The middle figure plots the displacement $\theta - \omega t$ over a full revolution of the oval, where θ is the angular position of the right-most tip of the oval. The schematic figures above show the corresponding position of the oval and its right-most tip. The oscillation near $0.05 - 0.15$ seconds corresponds to the opposite end (left-most tip) of the oval contacting the road. The large displacement near $0.2 - 0.27$ seconds corresponds to the right-most tip itself contacting the road. The bottom plot displays $\mathrm{Re}\,(e^{\lambda t})$, where λ is the eigenvalues corresponding to the fundamental mode. The similar frequency and rate of decay of the two plots near 0.1 seconds indicate the excitation of the fundamental mode is captured in the middle plot.

material are those of the author(s) and do not necessarily reflect the views of the National Science Foundation.

References

1. D.M. Ambrose and J. Wilkening, *Computation of time-periodic solutions of the Benjamin–Ono equation*, J. Nonlinear Sci. **20** (2010), 277–308.
2. J.M. Ball, *Convexity conditions and existence theorems in nonlinear elasticity*, Archives for Rational Mechanics and Analysis **63** (1977), 337–403.
3. J.M. Bass, *Three-dimensional finite deformation, rolling contact of a hyperelastic cylinder: Formulation of the problem and computational results*, Computers and Structures **26** (1987), 991–1004.
4. P.G. Ciarlet, *Mathematical elasticity*, North-Holland, 1988.
5. J.R. Dormand and P.J. Prince, *A family of embedded Runge-Kutta formulae*, Journal of Computational and Applid Mathematics **6** (1980), 19–26.
6. ———, *Practical Runge-Kutta processes*, SIAM Journal on Scientific and Statistical Computing **10** (1989), 977–989.
7. S. Govindjee and P.A. Mihalic, *Viscoelastic constitutive relations for the steady spinning of a cylinder*, Tech. Report UCB/SEMM-98/02, University of California Berkeley, Department of Civil Engineering, 1998.
8. S. Govindjee, T. Potter, and J. Wilkening, *Stability of spinning viscoelastic bodies at finite deformations*, (2013), (in submission).
9. S. Govindjee and S. Reese, *A presentation and comparison of two large deformation viscoelastic models*, ASME Journal of Engineering Materials and Technology **119** (1997), 251–255.
10. E. Hairer, S.P. Nørsett, and G. Wanner, *Solving ordinary differential equations I. Nonstiff problems*, Springer-Verlag, 1987.
11. R. Kennedy and J. Padovan, *Finite element analysis of steady and transiently moving/rolling nonlinear viscoelastic structure–II. Shell and three-dimensional simulations*, Computers and Structures **27** (1987), 249–257.
12. D.A. Knoll and D.E. Keyes, *Jacobian-free Newton–Krylov methods: a survey of approaches and applications*, Journal of Computational Physics **193** (2004), 357–397.
13. P. Le Tallec and C. Rahier, *Numerical models of steady rolling for non-linear viscoelastic structures in finite deformations*, International Journal for Numerical Methods in Engineering **37** (1994), 1159–1186.
14. J.T. Oden and R. Lin, *On the general rolling contact problem for finite deformations of a viscoelastic cylinder*, Computer Methods in Applied Mechanics and Engineering **57** (1986), 297–367.
15. J. Padovan, *Finite element analysis of steady and transiently moving/rolling nonlinear viscoelastic structure–I. Theory*, Computers and Structures **27** (1987), 249–257.
16. J. Padovan and O. Paramodilok, *Generalized solution of time dependent traveling load problem via moving finite element scheme*, Journal of Sound and Vibration **91** (1983), 195–209.
17. J. Padovan and O. Paramodilok, *Transient and steady state viscoelastic rolling contact*, Computers and Structures **20** (1985), 545–553.
18. T. Potter, *Dynamics and stability of rolling viscoelastic tires*, Ph.D. thesis, University of California, Berkeley, 2013.
19. J. Qi, J.R. Herron, K.H. Sansalone, W.V. Mars, Z.Z. Du, M. Snyman, and H. Surendranath, *Validation of a steady-state transport analysis for rolling treaded tires*, Tire Science and Technology (TSTCA) **35** (2007), 183–208.
20. S. Reese and S. Govindjee, *Theoretical and numerical aspects in the thermo-viscoelastic material behaviour of rubber-like polymers*, Mechanics of Time-Dependent Materials **1** (1998), 357–396.
21. ———, *A theory of finite viscoelasticity and numerical aspects*, International Journal of Solids and Structures **35** (1998), 3455–3482.
22. F. Sidoroff, *Un modèle viscoélastique non linéaire avec configuration intermédiaire*, Journal de Mécanique **13** (1974), 679–713.

23. J.C. Simo, *On a fully three-dimensional finite-strain viscoelastic damage model: Formulation and computational aspects*, Computer Methods in Applied Mechanics and Engineering **60** (1987), 153–173.
24. D. Viswanath, *Recurrent motions within plane Couette turbulence*, J. Fluid Mech. **580** (2007), 339–358.
25. J. Wilkening and J. Yu, *Overdetermined shooting methods for computing standing water waves with spectral accuracy*, Computational Science & Discovery **5** (2012), 014017.
26. M.O. Williams, J. Wilkening, E. Shlizerman, and J.N. Kutz, *Continuation of periodic solutions in the waveguide array mode-locked laser*, Physica D **240** (2011), 1791–1804.

Appendix A. Linearizations

Recall the linearized equations:

$$\begin{aligned}\int_{\mathcal{B}} \dot{\widehat{\boldsymbol{\phi}}} \cdot \zeta &= \int_{\mathcal{B}} \widehat{\boldsymbol{\nu}} \cdot \zeta \\ \int_{\mathcal{B}} \dot{\widehat{\boldsymbol{\nu}}} \cdot \eta &= \int_{\mathcal{B}} -\frac{1}{\rho_R}\widehat{\mathbf{P}} : D\eta + \int_{\Gamma_e} \frac{1}{\rho_r}\widehat{\mathbf{h}} \cdot \eta \\ \int_{\mathcal{B}} \dot{\widehat{\mathbf{b}}}_e : K &= \int_{\mathcal{B}} \left(\widehat{\boldsymbol{\ell}\mathbf{b}_e} + \widehat{\mathbf{b}_e\boldsymbol{\ell}^{\mathsf{T}}} - 2\widehat{\mathcal{V}(\boldsymbol{\tau}_e)\mathbf{b}_e}\right) : K\,.\end{aligned} \tag{A.1}$$

We need formulas for $\widehat{\mathbf{P}}, \widehat{\mathbf{h}}$, and $\dot{\widehat{\mathbf{b}}}_e$. This requires a series of computations. The first set culminates in the computation of $\widehat{\mathbf{P}_e}$:

$$\begin{aligned}\widehat{\mathbf{F}} &= D\widehat{\boldsymbol{\phi}} \\ \widehat{\mathbf{C}} &= \widehat{\mathbf{F}}^{\mathsf{T}}\mathbf{F} + \mathbf{F}^{\mathsf{T}}\widehat{\mathbf{F}} \\ \widehat{I_1} &= 2(\mathbf{F} : \widehat{\mathbf{F}}) \\ \widehat{I_3} &= 2I_3(\mathbf{F}^{-\mathsf{T}} : \widehat{\mathbf{F}}) \\ \widehat{\mathbf{F}^{-\mathsf{T}}} &= -\mathbf{F}^{-\mathsf{T}}\widehat{\mathbf{F}}^{\mathsf{T}}\mathbf{F}^{-\mathsf{T}} \\ \widehat{\mathbf{P}_e} &= \frac{\kappa}{2}(\widehat{I_3}\mathbf{F}^{-\mathsf{T}} + (I_3 - 1)\widehat{\mathbf{F}^{-\mathsf{T}}}) \\ &\quad + \mu(1-s)(\widehat{\mathbf{F}} - \widehat{\mathbf{F}^{-\mathsf{T}}}) + \mu s(\widehat{I_1}\mathbf{F} + I_1\widehat{\mathbf{F}} - (\mathbf{F}\widehat{\mathbf{C}} + \widehat{\mathbf{F}}\mathbf{C}) - 2\widehat{\mathbf{F}^{-\mathsf{T}}})\,.\end{aligned}$$

The second set gives $\widehat{\mathbf{P}_v}$:

$$\begin{aligned}\widehat{I_1^e} &= (\widehat{\mathbf{b}_e} : \mathbf{I}) \\ \widehat{I_3^e} &= I_3^e(\mathbf{b}_e^{-1} : \widehat{\mathbf{b}_e}) \\ \widehat{\boldsymbol{\tau}_e} &= \nu\left(\frac{\kappa}{2}\widehat{I_3}\mathbf{I} + \mu(1-s)\widehat{\mathbf{b}_e} + \mu s(\widehat{I_1^e}\mathbf{b}_e + I_1^e\widehat{\mathbf{b}_e} - (\mathbf{b}_e\widehat{\mathbf{b}_e} + \widehat{\mathbf{b}_e}\mathbf{b}_e))\right) \\ \widehat{\mathbf{P}_v} &= \boldsymbol{\tau}_e\widehat{\mathbf{F}^{-\mathsf{T}}} + \widehat{\boldsymbol{\tau}_e}\mathbf{F}^{-\mathsf{T}}\,.\end{aligned}$$

$\widehat{\mathbf{P}}$ is then given by

$$\widehat{\mathbf{P}} = \widehat{\mathbf{P}_e} + \widehat{\mathbf{P}_v}\,.$$

A third set of computations leads to $\dot{\widehat{\mathbf{b}}}_e$:

$$\begin{aligned}
\dot{\widehat{\mathbf{F}}} &= D\widehat{\boldsymbol{\nu}} \\
\widehat{\boldsymbol{\ell}} &= \dot{\widehat{\mathbf{F}}}\mathbf{F}^{-1} + \dot{\mathbf{F}}\widehat{\mathbf{F}^{-1}} \\
\widehat{\mathcal{V}(\boldsymbol{\tau}_e)} &= \frac{1}{2\mu\tau}\left(\widehat{\boldsymbol{\tau}_{\boldsymbol{e}}} - \frac{1}{2}(\operatorname{tr}\widehat{\boldsymbol{\tau}_{\boldsymbol{e}}})\mathbf{I}\right) + \frac{1}{4\kappa\tau}(\operatorname{tr}\widehat{\boldsymbol{\tau}_{\boldsymbol{e}}})\mathbf{I} \\
\dot{\widehat{\mathbf{b}}}_e &= \widehat{\boldsymbol{\ell}\mathbf{b}_e} + \widehat{\mathbf{b}_e\boldsymbol{\ell}^{\mathsf{T}}} - 2\widehat{\mathcal{V}(\boldsymbol{\tau}_e)\mathbf{b}_e} \\
&= (\widehat{\boldsymbol{\ell}}\mathbf{b}_e + \boldsymbol{\ell}\widehat{\mathbf{b}_e}) + (\widehat{\mathbf{b}_e}\boldsymbol{\ell}^{\mathsf{T}} + \mathbf{b}_e\widehat{\boldsymbol{\ell}^{\mathsf{T}}}) - 2(\widehat{\mathcal{V}(\boldsymbol{\tau}_{\boldsymbol{e}})}\mathbf{b}_e + \mathcal{V}(\boldsymbol{\tau}_{\boldsymbol{e}})\widehat{\mathbf{b}_e})\,.
\end{aligned}$$

Finally, we compute $\widehat{\mathbf{h}}$:

$$\begin{aligned}
\widehat{x_2} &= \widehat{\boldsymbol{\phi}_2} \\
\widehat{\mathbf{h}} &= -\delta\gamma'(-h - x_2)\widehat{x_2}\mathbf{e}_2\,.
\end{aligned}$$

University of California, Berkeley, CA 94720, USA

E-mail address: s_g@berkeley.edu, potter@math.berkeley.edu, wilkening@berkeley.edu